PNAS

Supporting Information for

pH-dependent structural transitions in cationic ionizable lipid mesophases and LNP core phases

Julian Philipp[8], Aleksandra Dabkowska[1], Anita Reiser[8], Kilian Frank[8], Rafał Krzysztoń[8], Christiane Brummer[8], Bert Nickel[8], Clement E. Blanchet[6], Akhil Sudarsan[7], Mohd Ibrahim[7], Svante Johansson[1], Pia Skantze[1], Urban Skantze[1], Sofia Östman,[2] Marie Johansson,[2] Neil Henderson,[3] Kjetil Elvevold[4], Bård Smedsrød[5], Nadine Schwierz[7], Lennart Lindfors[1] and Joachim O. Rädler[8*]

*Joachim Oskar Rädler (ORCID ID 0000-0002-5846-1489)
Email: raedler@lmu.de

This PDF file includes:

Symmetry and SAXS indexation of CIL/chol/buffer mesophases

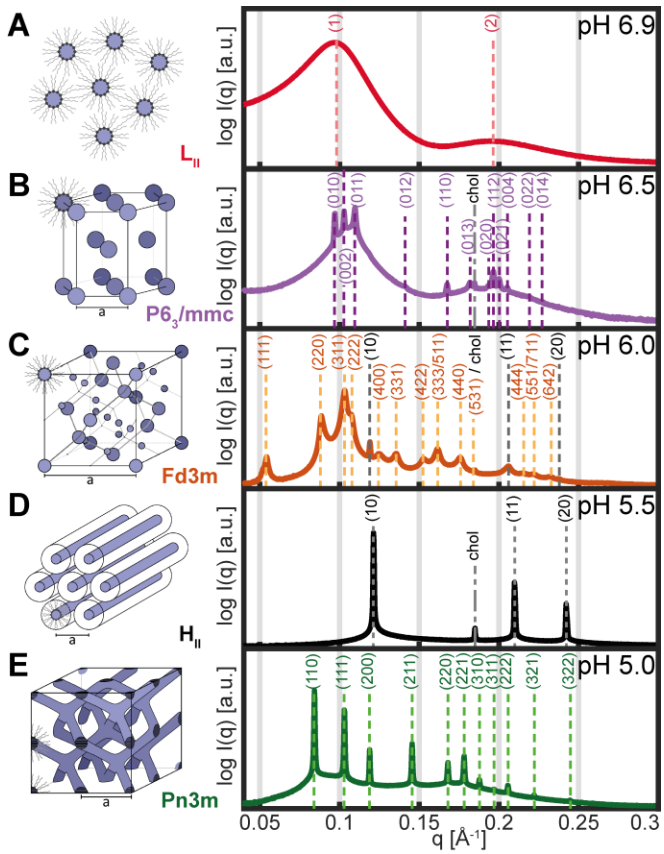

Figure S1. (A) Inverse micellar fluid isotropic, L_{II} (B) inverse micellar hexagonal with P6$_3$/mmc symmetry (C) inverse micellar cubic with Fd3m symmetry (D) inverse hexagonal, H_{II} (E) bicontinuous cubic, Pn3m

Preparation of bulk phases

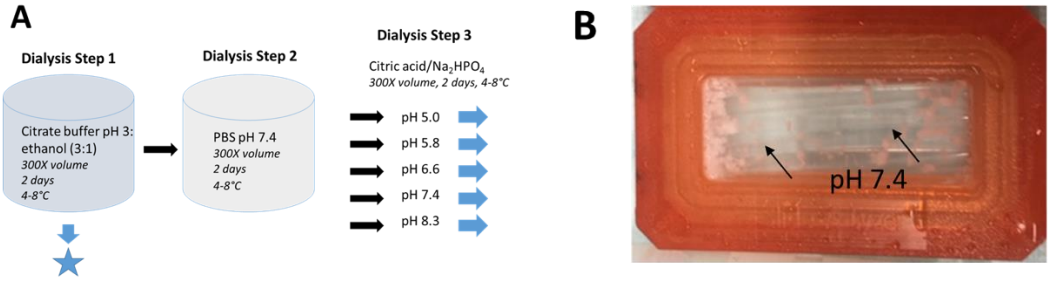

Figure S2. (A) Diagram of the dialysis steps followed for the production of lipid bulk phase. (B) Photograph of dialysis cassette containing precipitated core phases (arrows) in PBS, pH 7.4. The preparation mimics the LNP manufacturing conditions in the microfluidic mixer where the polyA:CIL complex forms. At these low pH conditions, the core phases of all CILs form disordered phases after two days of dialysis.

Reproducibility of bulk phases

While the results are generally consistent with the ordered hexagonal phase disappearing at pH 7.4, the location and amplitude of the broad peaks below 0.1 Å^{-1} are not reproducible between samples and between re-measurements of the same sample. Figure S2 shows one polyA-containing sample (same dialysis cassette) was re-measured in succession. The amplitude of the peak at 0.05 Å^{-1} was found to decrease with re-loading. Also, there appears to be a slight shift in the cholesterol peak.

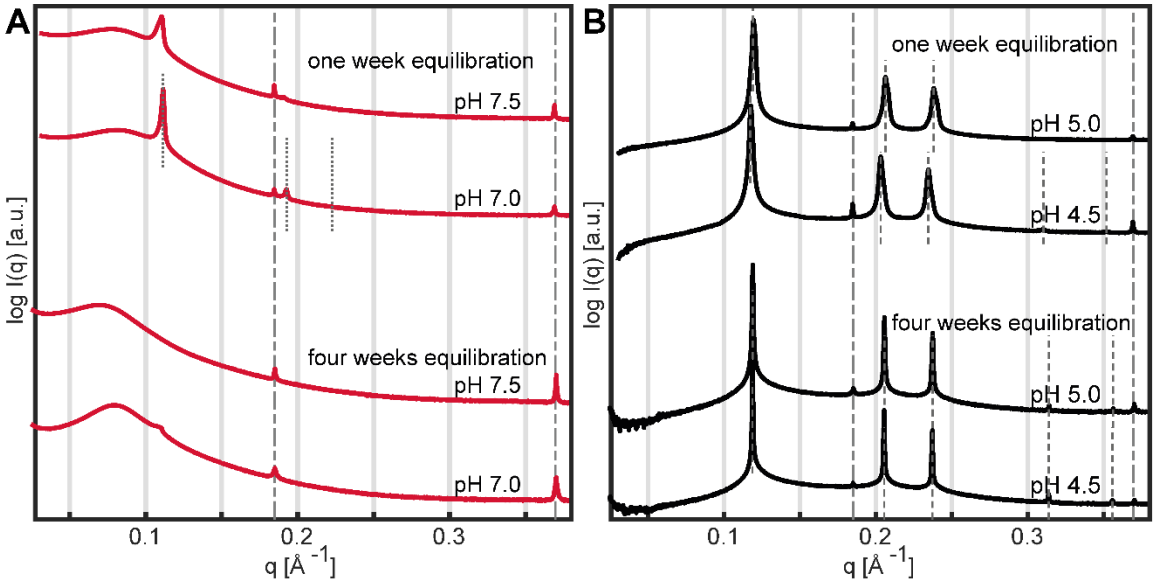

Figure S3. Comparison of bulk phase samples prepared following the same procedure but measured at different times. (A) At neutral pH the H_{II}^{C} phase disappears over time, possibly converting into the more stable L_{II}^{C} phase. (B) At low pH the H_{II} peaks become narrower, indicating an increase in domain size and therefore crystallization.

Encapsulation of polyA in the mesophases

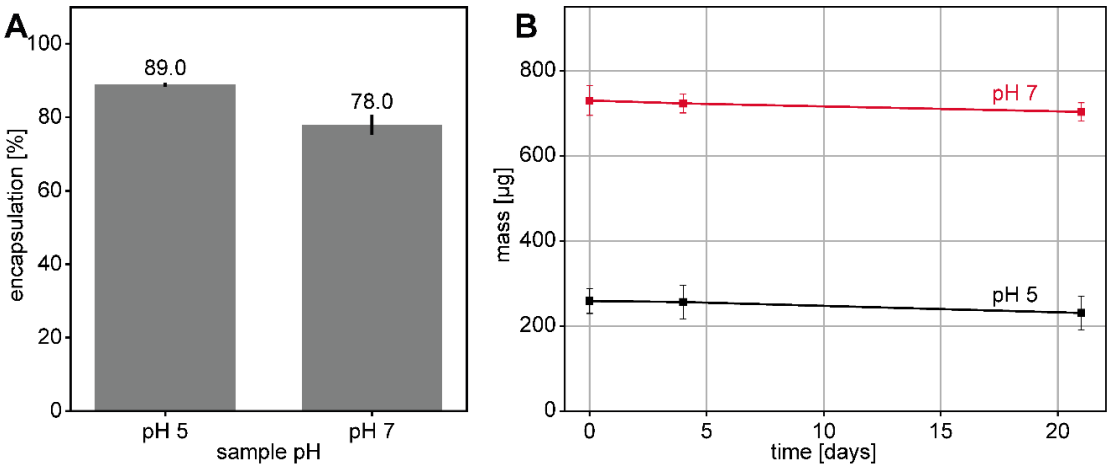

Figure S4. (A) For the bulk samples the polyA encapsulation was measured at pH 7 and pH 5 with two samples each. As expected the polyA encapsulation is higher with charged CIL compared to the encapsulation at neutral pH and therefore neutral charge of the CIL. The measurements were conducted by measuring the polyA content in the remaining supernatant after the dialysis to the respective pH value. (B) By measuring the polyA content in the supernatant at different time points after the dialysis, the release of polyA from the samples after the preparation was examined. Over the course of three weeks, almost no additional polyA was measured which shows that after the preparation only very little polyA diffuses out the bulk phases, regardless of the buffer pH. Each data point consists of five individual measurements of five different probes of the supernatant.

Simulation Methods

Simulation setup of inverse hexagonal (H_{II}) phase

To model the inverse hexagonal phase, we follow the procedure described in (1). A cylindrical water column surrounded by MC3 lipids and cholesterol was initially prepared using the CHARMM-GUI webserver (2). We assume that at the given pH, all MC3 molecules are charged. The mole fractions of MC3 and cholesterol was in the ratio 3:1. The setup so prepared was placed in a triclinic simulation box, which ensures a hexagonal lattice structure of the setup and its periodic images (**Fig. 5A**). To reproduce the experimental hexagonal lattice spacing, several simulations were first run by varying the number of waters per lipid (n_w) (**Fig. S5B**). We used 3 replicas of the system for each lattice spacing and the simulations were 200 ns long, discarding the first 50 ns for equilibration. To confirm that the systems are sufficiently equilibrated, we performed a longer simulation (1 μs) for the final lattice spacings (n_w = 12). The resulting electron density profiles remained unchanged (**Fig. S7E**) and we conclude that 200 ns are sufficient to yield converged results. The concentration of NaCl in the simulations was 150 mM and additional anions were included to neutralize the systems if necessary.

For H_{II}**,** each simulation box contained 150 MC3 lipids and 50 cholesterols. The corresponding number of water molecules were 1200, 2400, 3600 at n_w = 6, 12, 18. n_w = 12, best reproduced the experimental lattice spacing of 60 Å and was therefore used for further analysis and interpretation (see below).

Simulation setup of inverse micellar phase

To model the inverse micellar phase, we use a rhombic dodecahedron box with square faces to mimic a surrounding with twelve nearest neighbors. The Packmol package (3) was used to create a uniform water sphere surrounded by MC3 lipids and cholesterol. Here, we assume that at the given pH all MC3 molecules are uncharged. Similar to the hexagonal phase, we vary the molar ratios of water to CIL molecules (**Fig.S5C,D**). Each simulation box contained 75 MC3 lipids and 25 cholesterols. The corresponding number of water molecules were 600, 1000, 1200, 1600, 1800 at n_w = 6, 10, 12, 16, 18. The inverse micellar system with n_w = 16 was found to reproduce the lattice spacing of 60 Å (see below). Further analysis was performed on this system.

Simulation setup of the inverse micellar to inverse hexagonal transition

To understand the micellar to hexagonal transition with pH change, the equilibrated inverse micelle structure at n_w = 16 was used as starting structure. In a first step, the charge state of the MC3 head groups was changed from unprotonated to fully protonated. Subsequently, the system was energy minimized and equilibrated as described below. During the equilibration, the cationic MC3 head groups swing out into the water phase after a few hundred picoseconds. During the production run, the lipids reorder and the characteristic cylindrical water column of the hexagonal phase is formed after about 10 ns.

Lattice spacing as a function of hydration

In the MD Simulations, we varied the water content by choosing increasing molar ratios of water to CIL molecules (n_w). The results for the inverse hexagonal (H_{II}) phase and the inverse micellar (L_{II}) phase are shown in **Fig. S6A** and **Fig. S6B**, respectively. Based on the experimentally measured

lattice spacing of 60 Å, we selected the systems with n_w = 12 for inverse hexagonal phase simulations and n_w = 16 for inverse micelle simulations.

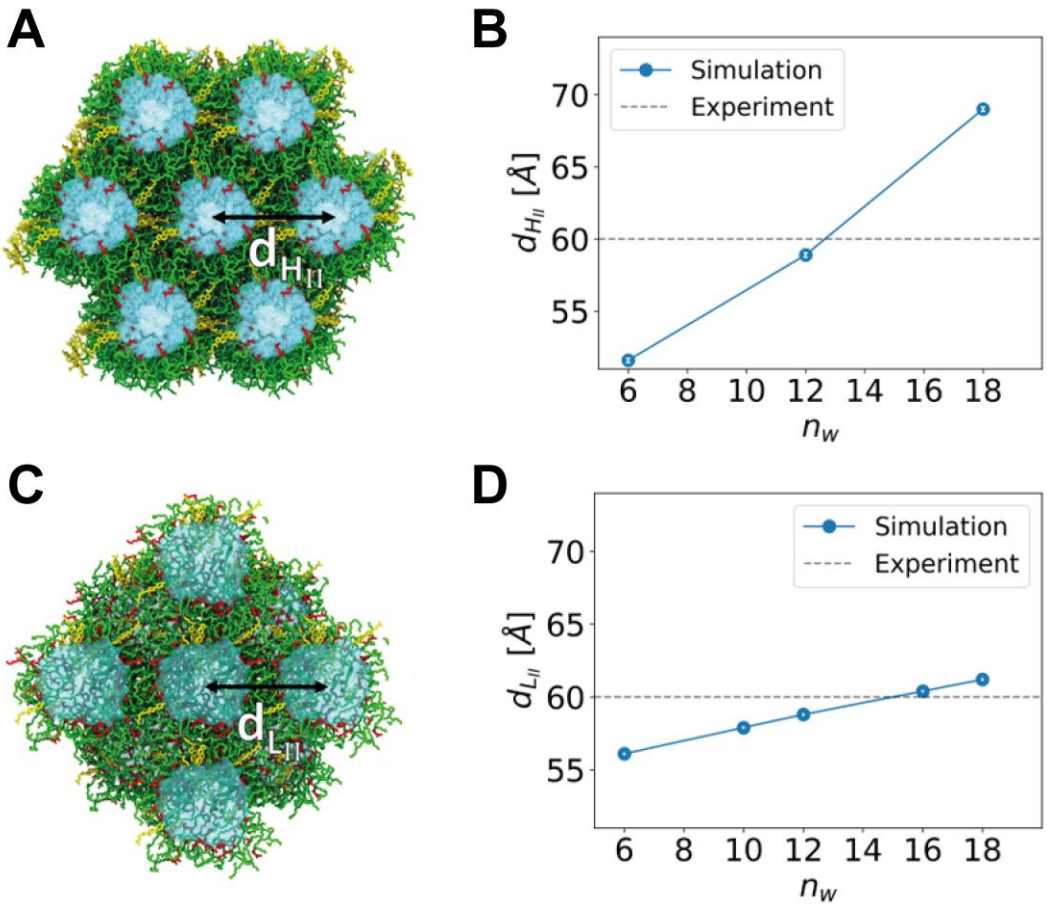

Figure S5. (A) Simulation snapshot of the inverse hexagonal phase in top view. The lattice spacing $d_{H_{II}}$ is given by the distance between the center of neighboring water wires. (B) Lattice spacing with increasing hydration for the H_{II} phase. The horizontal dashed line represents the experimental value of lattice spacing. Errors correspond to the standard deviation obtained from 3 independent simulations. Note that the error bars are smaller than the symbols. (C) Simulation snapshot of the inverse micellar phase. Each inverse micelle is surrounded by 12 neighboring inverse micelles. (D) Lattice spacing $d_{L_{II}}$ with increasing hydration for the L_{II} phase. Similar to B the horizontal dashed line represents the experimental value of lattice spacing and the errors correspond to the standard deviation obtained from 3 independent simulations.

Calculation of the effective volume fraction of water from MD simulations
The volume fraction of water ϕ_W is defined as the ratio of the volume of the water and the total volume of the system. In the MD simulations, the probability density function of finding an atom at a radial distance r is given by $p(r) = \rho_t(r)/\rho_0$ where $\rho_t(r)$ is the number density of the system along r and ρ_0 is the normalizing constant defined by $\int_0^\infty p(r)\, d^3r = 1$. Using the radial symmetry of the inverse hexagonal and micellar phase, the effective water volume fractions $\phi_w^{H_{II}}$ and $\phi_w^{L_{II}}$ were calculated from

$$\phi_w^{H_{II}} = \frac{\int_0^\infty p_w^{H_{II}}(r) d^3r}{\int_0^\infty p_t^{H_{II}}(r) d^3r} = \frac{\int_0^{r_{cut}} r\rho_w^{H_{II}}(r) dr}{\int_0^{r_{cut}} r\rho_t^{H_{II}}(r) dr}$$

$$\phi_w^{L_{II}} = \frac{\int_0^{\infty} p_w^{L_{II}}(r) d^3r}{\int_0^{\infty} p_t^{L_{II}}(r) d^3r} = \frac{\int_0^{r_{cut}} r^2 \rho_w^{L_{II}}(r) dr}{\int_0^{r_{cut}} r^2 \rho_t^{L_{II}}(r) dr}$$

where ρ_w and ρ_t are the number densities of water and the system. The results are shown in **Fig. S6** as function of n_w. Note that the water volume ratio calculated from the integrals becomes constant after a distance larger than r_{cut}. The values obtained by integration of the probability densities are 1-2% smaller compared to the calculation assuming an empirical water volume of 30.5 Å^3.

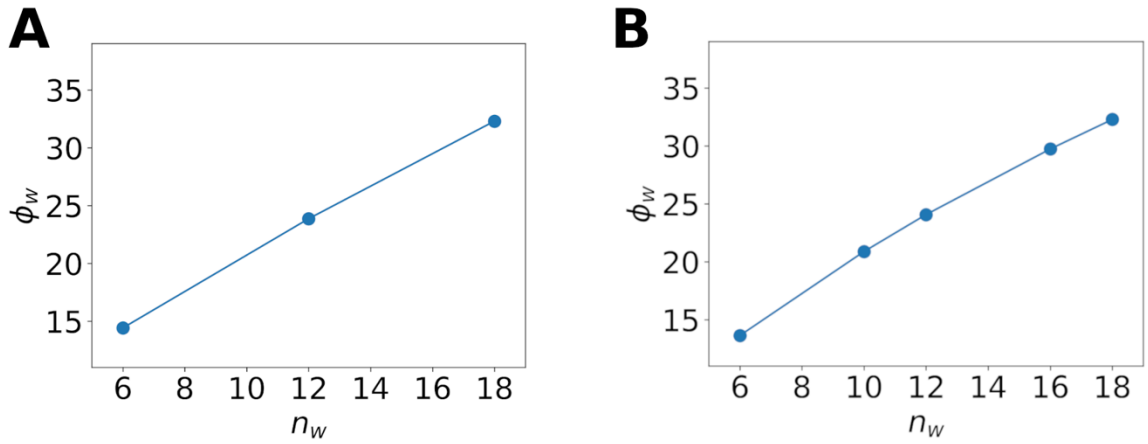

Figure S6. Variation of water volume fraction of the inverse hexagonal phase (A) and inverse micellar phase (B) with increasing hydration. For the H_{II} phase, the water volume fraction for n_w =12 is 23.9% and for the L_{II} phase with n_w =16 the volume fraction is 29.7%.

Electron Density Calculation

The electron density was calculated using custom python scripts based on MDAnalysis (4). For the inverse hexagonal phase, the simulation box was divided into concentric cylindrical shells oriented along the z-axis (i.e. along the water column orientation). The electron density in a given shell at distance r from the cylinder axis is given by

$$\rho_e(r) = \frac{\sum_i n_i z_i}{2\pi h r dr}$$

where n_i is the number of atoms of type i with z_i electrons, h is the box height in z-direction and dr = 0.5 Å is the width of the cylindrical shell. The summation is performed over all the atoms in a given shell.

Similarly, for the micellar phase, the box was divided into concentric spherical shells centered at the center of mass of the micelle. The electron density at a distance r is given by,

$$\rho_e(r) = \frac{\sum_i n_i z_i}{4\pi r^2 dr}$$

To confirm the simulation setup and binning for the electron density profile, we calculated the water density as function of the distance from the water wire (inverse hexagonal phase) or center of water sphere (inverse micelle phase). The value close to the center is identical to the literature value for bulk TIP3P water (5).

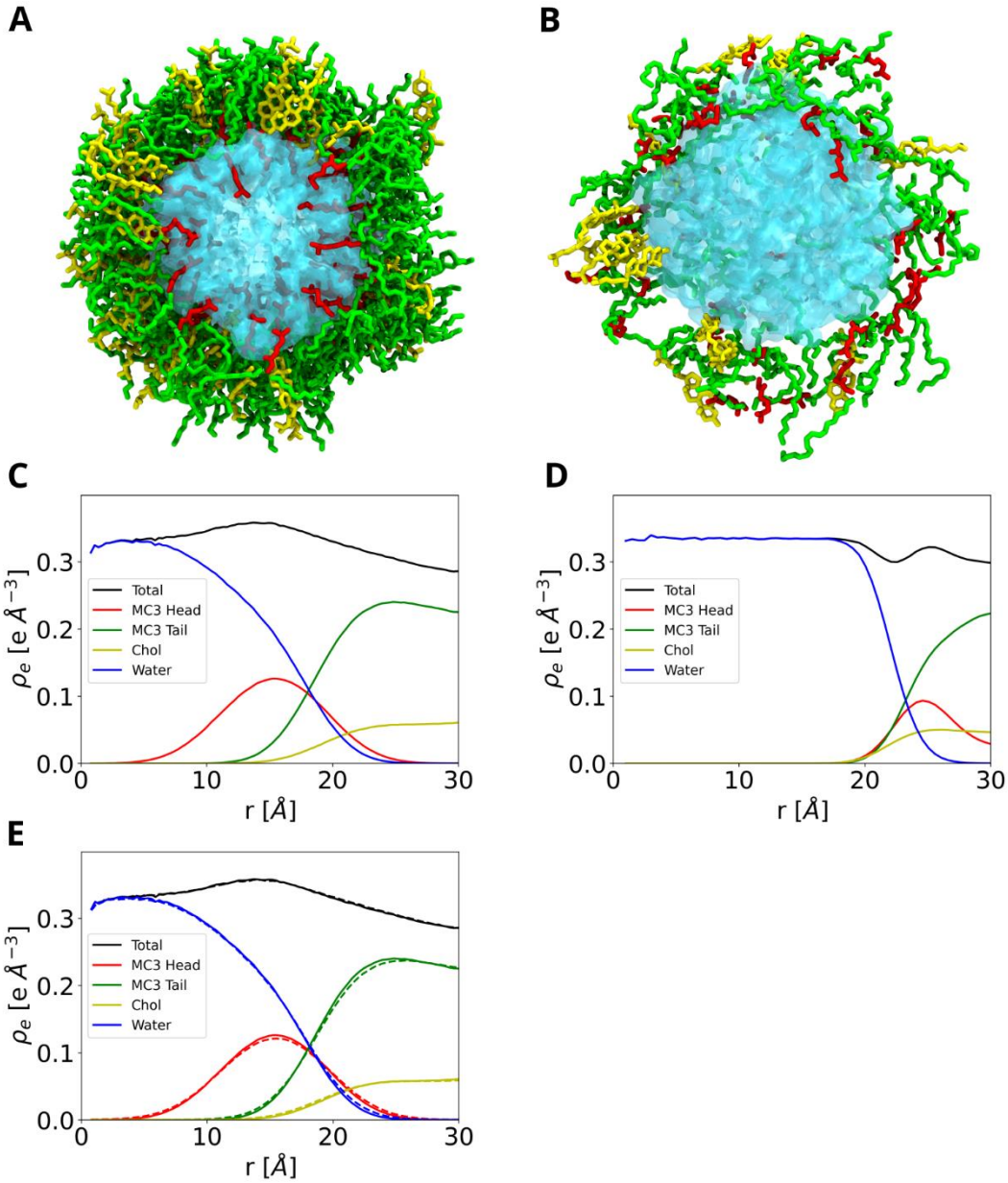

Figure S7. Simulation snapshots and electron densities for a single water column and a single inverse micelle. (A) Cross-section of the simulation box from the H_{II} phase (top view). (B) Cross-section of the simulation box for an inverse micelle from the L_{II} phase. Water is shown in blue, ionizable headgroups and tails of MC3 are shown in red and green, respectively. Cholesterol is shown in yellow. (C,D) Electron density profiles of the unit cell H_{II} including the contributions from neighboring micelles. Note that the headgroup of the protonated MC3 sticks into water in the H_{II} phase. The uncharged MC3 headgroup hides in the lipid region in the L_{II} phase. (E) To provide insights into the convergence of the H_{II} phase, the results after 200 ns (solid) and 1 µs (dashed) are shown.

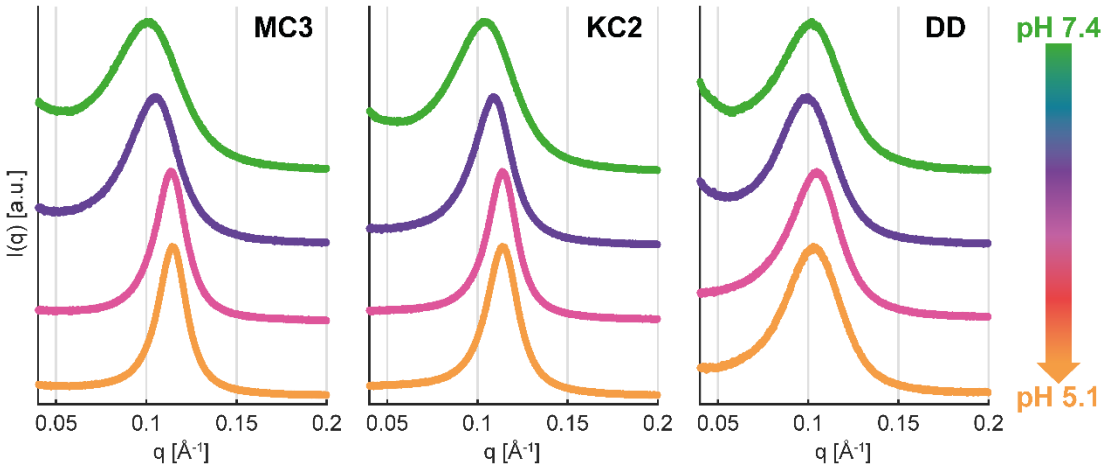

Figure S8. SAXS scattering curves of lipid nanoparticles containing eGFP mRNA. The plot shows a more significant pH-dependent peak position shift for LNPs with MC3 and KC2 compared to DD. The peak positions are plotted in **Fig.4E** of the main publication. Dispersions of LNPs (at 3-6 mg/mL mRNA concentration in McIlvaine buffer) were measured in quartz capillaries. The scattering background was subtracted using reference buffer measurements.

Fluorescence anisotropy measurements of DPH as a function of pH at 37 °C for LNPs

1,6-Diphenyl-1,3,5-hexatriene (DPH) was obtained from Fluka (lot 1054132). McIlvaine buffers of pH 3, 4, 5, 5.8, 6.6, 7.4 and 8 was prepared by mixing appropriate volumes of 0.05 M citric acid and 0.1 M Na_2HPO_4 followed by five times dilution with water and 1.5 M NaCl to obtain 0.15 M NaCl in the final solution. LNP samples in McIlvaine buffers were prepared at 40 μM lipid and 0.4 μM DPH and, also, corresponding samples without DPH for background correction. DPH/buffers were prepared by 1000-fold dilution of 0.5 mM DPH (acetonitrile) in each buffer. For each sample: 1600 μl DPH/buffer (or only buffer) +330 μl buffer +x μl LNP +(70-x) μl PBS. LNP/DPH samples were prepared and measured in triplicate while background samples were only measured once. The LNP samples were incubated over night at room temperature in the dark, followed by incubation at 37 °C for 8 minutes before measurements. The fluorescence intensity was measured with a PerkinElmer LS55 Luminescence Spectrometer at 37 °C with Ex/Em wavelengths= 360/430 nm. Fluorescence anisotropy, *r*, was calculated from the fluorescence intensities with polarizer settings HV (horizontal, vertical), HH, VV and VH as described in the supplementary information. The resulting r(pH) dependence was fitted by the Henderson-Hasselbalch equation.

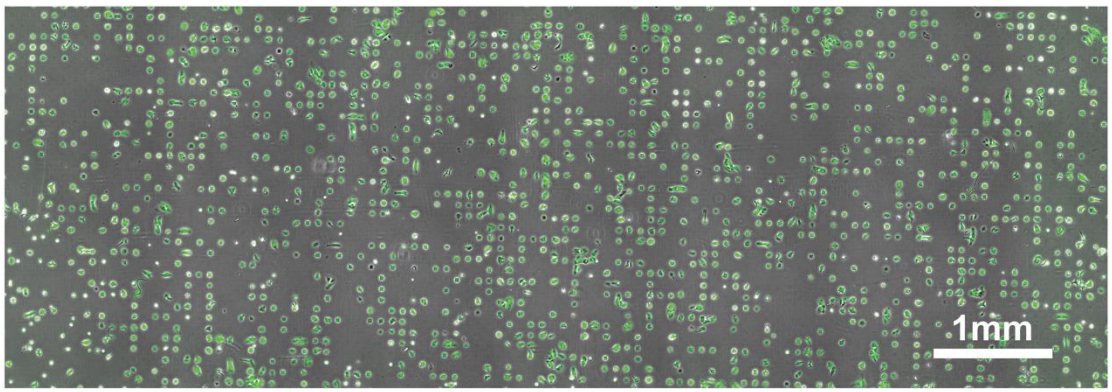

Figure S9. Expression kinetics and efficiency of CIL mediated transfection. (A) Individual cells expressing eGFP (green) on a micropatterned array 10 h after transfection (see also (6)).

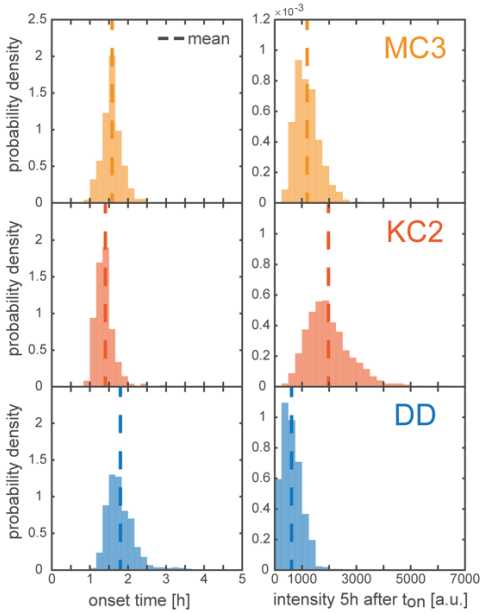

Figure S10. Onset time distribution and expression level after 5h Histograms of the eGFP onset time distribution of MC3 (orange) KC2 (red), and DD (blue) mediated transfection.

Lipid phase	Miller indices (hkl)	a/d_{hkl}	m_{hkl}
$Pn3m$	$(110), (111), (200), (211), (220), \ldots$	$\sqrt{h^2+k^2+l^2}$	$\sqrt{2}, \sqrt{3}, 2, \sqrt{6}, \sqrt{8}, \ldots$
H_{II}	$(10), (11), (20), (21), (30), \ldots$	$\sqrt{h^2+k^2+hk}$	$1, \sqrt{3}, 2, \sqrt{7}, \sqrt{9}, \ldots$
$Fd3m$	$(111), (220), (311), (222), (400), \ldots$	$\sqrt{h^2+k^2+l^2}$	$\sqrt{3}, \sqrt{8}, \sqrt{11}, \sqrt{12}, \sqrt{16}, \ldots$
$P6_3/mmc$	$(010), (002), (011), (012), (110), \ldots$	$\frac{4}{3}(h^2+k^2+hk)+\frac{3}{8}l^2$	$\sqrt{4/3}, \sqrt{3/2}, \sqrt{41/24}, \sqrt{17/6}, 4, \ldots$

Table S1. Miller indices of the measured lipid phases.

Lipid Phase	a	d_{NN}
$Pn3m$	$\frac{2\pi\, m_{hkl}}{q_{hkl}}$	$\frac{a}{\sqrt{2}}$
H_{II}	$\frac{4\pi\, m_{hkl}}{\sqrt{3}\, q_{hkl}}$	a
$Fd3m$	$\frac{2\pi\, m_{hkl}}{q_{hkl}}$	$\frac{a}{\sqrt{8}}$
$P6_3/mmc$	$\frac{2\pi\, m_{hkl}}{q_{hkl}}$	a

Table S2. Formula of the lattice constant a and the nearest neighbor distance d_{NN} for the measured lipid phases.

Movie S1 (separate file). The video starts with a 90° round view of the inverse micellar phase (L_{II}) with 12 nearest neighbors. All ionizable MC3 lipids are neutral. Subsequently, the cross section of the L_{II} phase is shown. Mimicking the change in pH, the MC3 lipids are protonated and the molecular dynamics simulations start. The MC3 head groups (red) quickly enter the water phase. Subsequently, the topology changes from L_{II} to H_{II} and the water columns are formed. The dynamics stops and a 90° rotation of the inverse hexagonal phase (H_{II}) is shown. In the video, head and tail groups of the MC3 lipids are shown in red and green, respectively. Water is shown in cyan and cholesterol in yellow

SI References

1. M. Ramezanpour, *et al.*, Structural Properties of Inverted Hexagonal Phase: A Hybrid Computational and Experimental Approach. *Langmuir* **36**, 6668–6680 (2020).
2. S. Jo, T. Kim, V. G. Iyer, W. Im, CHARMM-GUI: A web-based graphical user interface for CHARMM. *J. Comput. Chem.* **29**, 1859–1865 (2008).
3. L. Martínez, R. Andrade, E. G. Birgin, J. M. Martínez, PACKMOL: A package for building initial configurations for molecular dynamics simulations. *J. Comput. Chem.* **30**, 2157–2164 (2009).
4. N. Michaud-Agrawal, E. J. Denning, T. B. Woolf, O. Beckstein, MDAnalysis: A toolkit for the analysis of molecular dynamics simulations. *J. Comput. Chem.* **32**, 2319–2327 (2011).
5. C. Vega, J. L. F. Abascal, Simulating water with rigid non-polarizable models: a general perspective. *Phys. Chem. Chem. Phys.* **13**, 19663 (2011).
6. A. Reiser, D. Woschee, S. M. Kempe, J. O. Raedler, Live-cell Imaging of Single-Cell Arrays (LISCA) - a Versatile Technique to Quantify Cellular Kinetics. *Jove-J. Vis. Exp.*, e62025 (2021).